Experimental and numerical analysis of the flanging process by SPIF

To cite this article: JA López-Fernández *et al* 2018 *J. Phys.: Conf. Ser.* **1063** 012086

View the article online for updates and enhancements.

IOP ebooks™

Bringing you innovative digital publishing with leading voices to create your essential collection of books in STEM research.

Start exploring the collection - download the first chapter of every title for free.

Experimental and numerical analysis of the flanging process by SPIF

JA López-Fernández, G Centeno[(*)], AJ Martínez-Donaire, D Morales-Palma, C Vallellano

Department of Mechanical and Manufacturing Engineering, School of Engineering, University of Seville, Camino de los Descubrimientos s/n 41092, Sevilla (Spain).
[(*)] Correspondence: gaceba@us.es

Abstract. This paper analyses the flangeability of AA2024-T3 sheets using single point incremental forming (SPIF). With this purpose, a series of process parameters is considered including flange length and width, tool radius and spindle speed. An initial experimental campaign is carried out for the evaluation of the limiting strain states of the flanges within the material forming limit diagram (FLD). Numerical modelling through finite element analysis (FEA) is used in order to provide a better understanding of the sheets flangeability and forming conditions that either allow manufacturing or lead to failure in this process using concave dies. The capability of the SPIF process to improve formability is discussed.

Keywords: FLD, SPIF, flangeability, failure, FEA.

1. Introduction

Incremental sheet forming (ISF) processes, and especially its dieless variant known as single point incremental forming (SPIF), have been intensively studied within the forming community during the last few decades. The most attractive advantage of this process is its capability for enhancing the formability of the sheet up to the fracture forming limit (FFL) of the material, thus allowing stable plastic deformation above the conventional forming limit curve (FLC). Many systematic studies have been carried out in order to analyse this enhancement of formability both for metallic and polymeric materials, as discussed in the recent review paper by McAnulty et al. [1].

Although this technology has not a high industrial implantation yet, SPIF have been used for different technological applications and processes. For instance, research has been focused for the last few years on the production of hole-flanges by SPIF [2]. In this sense, the authors have recently presented a single-stage variant of this process [3], which allows reducing the production time, one of the main disadvantages of ISF. In this context, the work of Voswinckel et al. [4] was pioneer in applying SPIF for flanging of concave (stretch) and convex (shrink) open geometries, analyzing the capability of the SPIF process for increasing the formability in the manufacturing of flanges or flangeability.

In this technological context, this study is a preliminary attempt towards establishing the flangeability of metallic sheets using SPIF within a range of process parameters including flange length and width, tool radius and step down among others. The material is the AA2024-T3 sheet, a low formability aluminum alloy intensively used in the aeronautical sector. An experimental campaign for analyzing the strain states of the flanges using circle grid analysis is performed. Besides, a numerical investigation through finite element analysis (FEA) is considered in order to have a better understanding of the forming conditions that either allow manufacturing or lead to failure in this process using concave dies. The capability of SPIF to improve the intrinsically low formability of this materials is discussed.

2. Material characterization

This section presents the mechanical characterization of 1.2 mm thickness AA2024-T3 sheets, providing the mechanical properties and the flow curve of the material in section 2.1 as well as the limit strains represented through the FLD of the material in section 2.2.

2.1. Mechanical properties

Table 1 include the mechanical properties of the sheets obtained by means of tensile tests. This table provides the average yield stress (σ_Y), the ultimate tensile strength (σ_{UTS}), the modulus of elasticity (E), the Poisson's ratio (v) and the Lankford coefficients of anisotropy (r_θ). Further information regarding the determination of these mechanical properties can be found elsewhere [5].

Table 1. Mechanical properties.

σ_Y (MPa)	σ_{UTS} (MPa)	E (GPa)	v	$r_{0^o\text{-}45^o\text{-}90^o}$
335	526	66.7	0.33	0.84-1.00-0.77

The stress-strain flow curve of the material was fitted at 0º using a Swift's power law as follows:

$$\bar{\sigma} = 814.04 \left(0.025 + \bar{\varepsilon}^P \right)^{0.245} \quad \text{(MPa)} \tag{1}$$

where $\bar{\varepsilon}^P$ is the value of the equivalent plastic strain.

2.2. Forming limit diagram

Nakazima tests using a hemispherical punch of Ø100 mm were performed in a universal sheet testing machine Erichsen 142-20 under standard ISO 12004-2:2008 [6] testing conditions. The velocity of the punch was set to 1 mm/s and the lubrication at the punch-sheet interface was assured by the use of Vaseline + PTFE + Vaseline. The digital image correlation (DIC) measurement system ARAMIS® was utilized for evaluating the strain paths at the outer surface of the tested sheets until the onset of failure. The procedure proposed by the standard ISO for determining the onset of necking expressed by the forming limit curve (FLC) was performed for the four strain paths considered, as well as a time-dependent methodology recently proposed by the authors [7]. In none of these cases was found an evidence of localized necking, thus being the failure of the material controlled by direct ductile fracture in the absence of necking. In this regard, the limit strains within the FLD are defined for the mode I of fracture mechanics by the fracture forming line (FFL) of the material, as represented in Figure 1.

Notice that the procedure for constructing the FFL depicted in Figure 1 consists on the measurement of thickness at fracture at several places along the crack in order to obtain the average thickness strain. The average major strain at fracture is calculated by volume constancy as follows:

$$\bar{\varepsilon}_{1,f} = \frac{-\bar{\varepsilon}_{3,f}}{(1 + \beta^*)} \tag{2}$$

where $\bar{\varepsilon}_{3,f}$ is the average thickness strain measured and $\beta^* = d\varepsilon_2 / d\varepsilon_1$ is the local strain ratio evaluated at the last image recorded by ARAMIS®. Besides, some specimens were cut perpendicularly to the crack and the thickness was measured from a profile view, validating the above described thickness measurements along the crack (notice the absence of necking in the microscopic image provided in Figure 1 for the case of the biaxial strain path), as previously performed by the authors in [8].
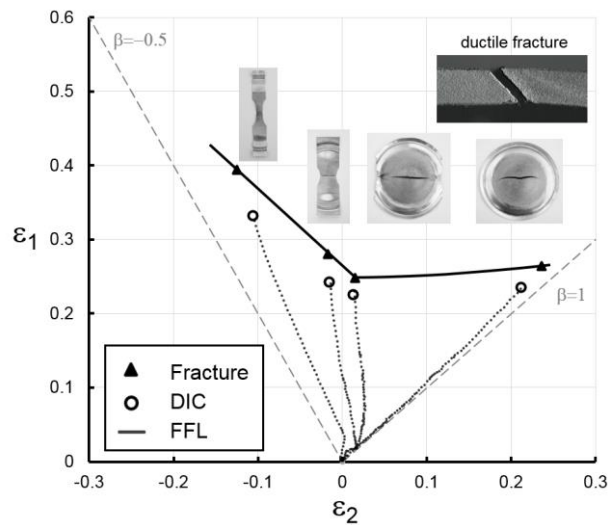
Figure 1. FLD of the material represented by the FFL as a consequence of the failure by ductile fracture in the absence of local necking.

3. Experimental plan of incremental flanging

This section presents the experimentation regarding the process for obtaining concave flanges deformed under stretching conditions by SPIF using concave dies. Section 3.1 presents the process setup as well as the range of process parameters considered for this preliminary investigation whereas section 3.2 presents the process window carried out during the flanging experimental plan.
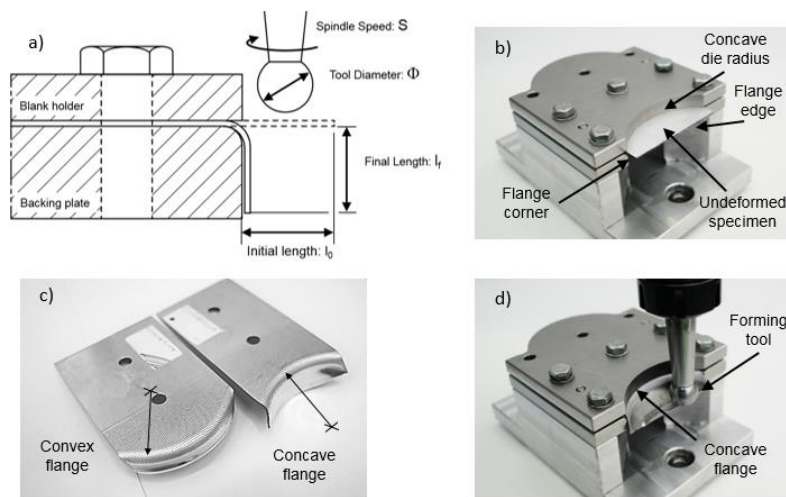
Figure 2. (a) Schematic process representation, (b) concave flange setup, (c) concave and convex flanges and (d) concave flange after SPIF performed with a die radius (R_{die}) of 45 mm.

3.1. Stretch flanging process by SPIF

Figure 2a depicts a schematic representation of the flanging process, being the concave flange setup with a die radius (R_{die}) of 45 mm and the resulting flange shown in Figures 2b and 2d respectively. Although concave flanges are deformed under stretching conditions and fail usually by fracture, convex flanges are submitted to circumferential compression and fail by instability due to shrinking (Notice that this work does not focus on convex flanging). Table 2 presents the range of process parameters selected for performing the experimental plan, where Φ_{tool} is the tool radius, S the spindle speed, l_o the initial flange length, w_0 the initial width and Δz the step down per pass.

Table 2. Process parameter in the flanging process.

R_{die} (mm)	Φ_{tool} (mm)	S (rpm)	l_o (mm)	w_0 (mm)	Δz (mm)
45	**12** / 20	**20**	**15 / 20 / 25**	**36/ 45 / 54 / 63 / 72**	0.2 / **0.4**

3.2. Flanging experimental plan

Corresponding to the process parameters presented in the previous section, Table 3 exposes the initial experimental plan of the flanging process by SPIF considering the parameters represented in bold characters in Table 2. This table indicates if the specimen is successfully manufactured into a concave flange (no failure - N.F.) or if fractures either at the flange corners (failure at flange corners - F.C.) or at the flange edge (failure at the flange edge - F.E.).

Table 3. Initial experimental plan of the flanging process by SPIF.

l_o (mm)	w_0 (mm)				
	36	**45**	**54**	**63**	**72**
15	N.F.	N.F.	N.F.	N.F.	N.F.
20	N.F.	N.F.	N.F.	N.F.	**N.F.**
25	N.F.	N.F.	F.C.	F.C.	**F.E.**

As can be seen, the pair of initial length and width ($l_{0,f}$, $w_{0,f}$) equal to (25 mm, 72 mm) is the case that controls failure by fracture at the edge of the flange. Then for the highest pair of values (l_0, w_0) defining the successful manufacturing of a flange in Table 3, i.e. (20 mm, 72 mm), two additional tests were conducted considering (i) a tool diameter of 20 mm and (ii) a step down of 0.4 mm (both values included in the range of process parameters presented in Table 2), resulting (i) in the successful flange (N.F.) and (ii) a fractured flange at edge (F.E.) respectively. These relevant cases are defined as case 1 to case 4 in Table 4 respectively. It must be noticed that the results obtained are not in perfect agreement with the general influence of these parameters in SPIF (see references [1] or [8]) as far as a small tool diameters should result in higher formability whereas the variation of the step down in the range of 0.1 to 0.5 mm does not usually play a relevant role in terms of formability. For this reason, with the aim of providing a better understanding of this unusual behavior in terms of formability, the stress/strain states attained in concave flanging by SPIF for these 4 cases in Table 4 are analyzed in detail in the following sections.

Table 4. Process parameters in the different cases analysed.

	Flange	l_o (mm)	w_0 (mm)	Φ_{tool} (mm)	Δz (mm)
Case 1	F.E.	25	72	12	0.4
Case 2	N.F.	20	72	12	0.4
Case 3	N.F.	20	72	20	0.4
Case 4	F.E.	20	72	12	0.2

4. Finite element modelling

A numerical model of the flanging process described in section 3.1 was carried out and simulated for the 4 cases in Table 4 using ANSYS/LS-DYNA® with the objective of analyzing virtually the process and thus providing a better understanding of the sheet flangeability and forming conditions in this process using concave dies. This commercial software allows a Finite Element Analysis (FEA) based on explicit dynamics computation.

The numerical model was developed using solid shell elements SHELL163 with 5 through-thickness points of integration, having the homogeneously distributed mesh an initial size of 1 mm resulting in around 4000 elements. The punch and the concave die are considered to be rigid bodies, and the displacements and rotations of the shell element under the surface of the blank holder were supposed to be fully restricted (clamping boundary conditions). The punch follows the real trajectory of the experiments carried out in the CNC machining center. The metal sheet behaves as an elastic-plastic rate-independent material with isotropic hardening. The elastic-plastic behavior is modelled considering 3 parameters Barlat's anysotropy and following the Swift's power law presented in section 2.1. Figure 3a depicts the mesh of the initial FE model whereas Figure 3b shows the contour of major principal strains on the deformed shape after the flanging process by SPIF for the case 2 defined in Table 3. To conclude, it is worth mentioning that the central processing unit (CPU) time for a typical analysis was approximately 15 hours on a computer using 8 Intel Xeon® E3 v6 CPUs (3 GHz) processors.
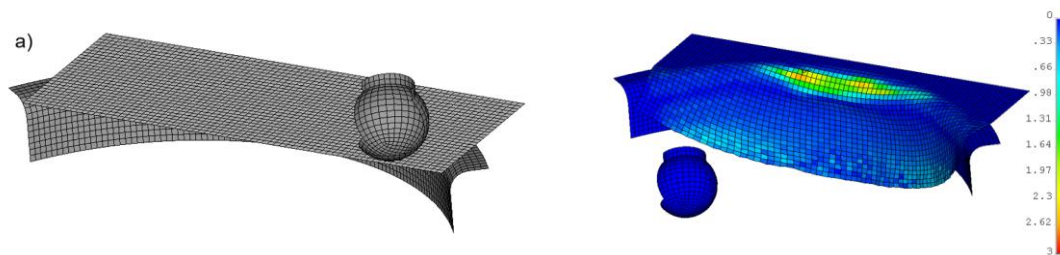
Figure 3. (a) Initial FE model and (b) contour of major strain after the flanging process.

5. Results

Figure 4a depicts the FE predicted strains path evolution vs. the experimental evolution evaluated using ARGUS® along a section ending at the zone of the flange edge with the highest level of equivalent strains (see the caption at the down-left corner) for case 2 in Table 4 corresponding to a successful flange. As can be seen, the numerical prediction is in good agreement with the experimental results. Besides, the principal strains evaluated using ARGUS® for case 1 (leading to fracture at the flange edge) are also provided in Figure 4. As can be seen, the strain path in this case reaches a region slightly above the FFL, being the onset of failure located at a zone close to the flange edge (caption at up-right corner).
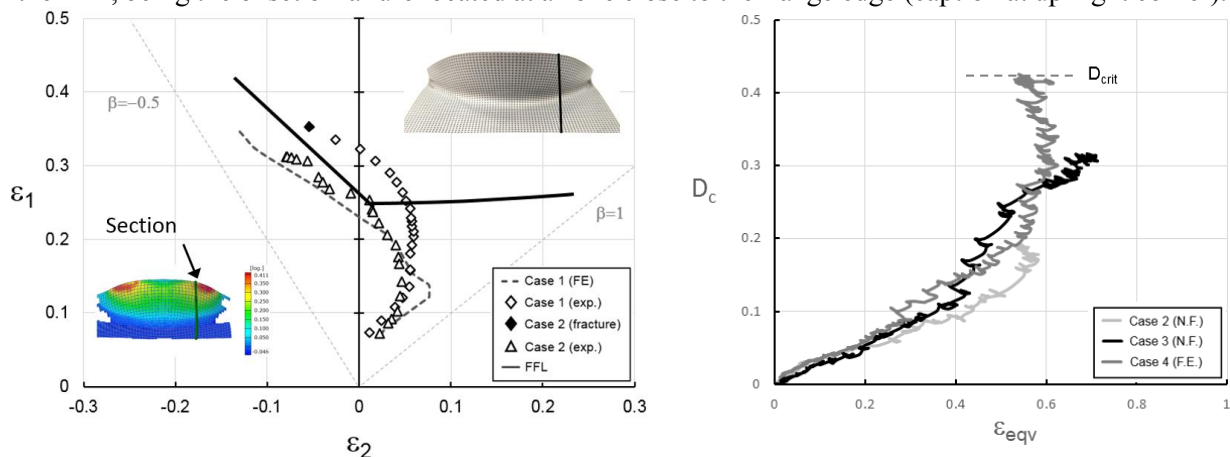
Figure 4. (a) FE strains path prediction vs experimental results and (b) accumulated damage

Finally, the FE modelling permits understanding the influence of process parameters in formability reported in Table 4, which either allow the successful manufacturing or lead to fracture at the flange edge. As failure is reached by direct ductile fracture under in-plane tension corresponding to the mode I of fracture mechanics, the non-coupled damage (*D*) criterion of McClintock [9] based on void growth applies as expressed in Equation 3 (see [8] for extended information and references in this regard), where the ratio of the hydrostatic (σ_H) to the equivalent stress ($\bar{\varepsilon}$) represent the stress triaxiality.

$$D = \int_0^{\bar{\varepsilon}} \frac{\sigma_H}{\bar{\sigma}} \, d\bar{\varepsilon} \tag{3}$$

Figure 4b depicts the McClintock's accumulated damage versus equivalent strain for cases 2 to 4 (those considering an initial length l_0 of 20 mm). As can be seen, the highest level of accumulated damage is attained in case 4 (tool diameter 12 mm, step down of 0.2 mm/pass), allowing setting a numerical upper limit assessment of the critical damage (D_{crit}). Regarding the cases with no fracture, case 2 (tool diameter 12 mm, step down 0.4 mm/pass) is the case with a lowest accumulated damage, whereas case 3 (tool diameter 20 mm, step down 0.4 mm/pass) presents an intermediate value not reaching the accumulated damage required to activate fracture. It can be thus concluded that, although the influence in formability of the tool radius seems to be the same that in other SPIF processes, i.e. a lower tool diameter a higher formability (or a lower accumulated damage), in flanging by SPIF the step down seems to play a relevant role in terms of formability that should be analysed in more detail.

Conclusions

This research work presented a preliminary analysis of the flangeability of AA2024-T3 sheets using SPIF. With this purpose, the influence of a series of process parameters including flange length and width, tool radius and step down was considered. A FEA was used for evaluating the sheet flangeability within the material FLD. The resulting prediction was validated using experimental results based on automatic circle gird analysis. The capability of the numerical model to assess the strain paths within the principal strain space was demonstrated, allowing the estimation of accumulated damage and the possibility of establishing an upper bound assessment for the critical damage for the process, which would establish the flangeability and forming conditions that either allow manufacturing or lead to failure in this process using concave dies. The results show that although the influence in formability of the tool radius seems to be as usual in incremental sheet forming, the step down seems to play a relevant role in terms of formability in concave flanging by SPIF.

References

[1]   McAnulty T, Jeswiet J, Doolan M (2017) Formability in single point incremental forming: A comparative analysis of the state of the art. CIRP Journal of Manufacturing Science and Technology 16: 43-54.

[2]   Silva MB, Bay N, Martins PAF (2016) Hole-flanging by single point incremental forming. Materials Forming and Machining, Woodhead/Elsevier, 25-50.

[3]   Borrego M, Morales-Palma D, Martínez-Donaire AJ, Centeno G, Vallellano C (2016) Experimental study of hole-flanging by single-stage incremental sheet forming. Journal of Materials Processing Technology, 237: 320-330.

[4]   Voswinckel H, Bambach M, Hirt G (2015), Improving geometrical accuracy for flanging by incremental sheet metal forming. International Journal of Material Forming 8(3):391-399.

[5]   Vallellano C, Morales D, García-Lomas FJ (2008) A study to predict failure in biaxially stretched sheets of Aluminum alloy 2024-T3, Materials and Manufacturing Processes, 23:303-310.

[6]   ISO 12004-2:2008 (2008), Metallic Materials-Sheet and Strip-Determination of Forming Limit Curves in Laboratory.

[7]   Martínez-Donaire AJ, García-Lomas FJ, Vallellano C (2014) New approaches to detect the onset of localised necking in sheets under through-thickness strain gradients. Materials & Design 57:135-45.

[8]   Centeno G, Martínez-Donaire AJ, Bagudanch I, Morales-Palma D, Garcia-Romeu M, Vallellano C (2017) Revisiting formability and failure of AISI304 sheets in spif: Experimental approach and numerical validation. Metals 7:531.

[9]   McClintock FA (1968) A criterion for ductile fracture by the growth of holes, Journal of Applied Mechanics, 35(2):363–371.